

See discussions, stats, and author profiles for this publication at: <https://www.researchgate.net/publication/11870739>

High-frequency (140-GHz) time domain EPR and ENDOR spectroscopy: the tyrosyl radical-diiron cofactor in ribonucleotide reductase from yeast.

ARTICLE *in* JOURNAL OF THE AMERICAN CHEMICAL SOCIETY · MAY 2001

Impact Factor: 12.11 · Source: PubMed

CITATIONS

35

READS

23

6 AUTHORS, INCLUDING:



H. Nguyen

California Institute of Technology

17 PUBLICATIONS 745 CITATIONS

SEE PROFILE



Robert G Griffin

Massachusetts Institute of Technology

454 PUBLICATIONS 24,726 CITATIONS

SEE PROFILE

High-Frequency (140-GHz) Time Domain EPR and ENDOR Spectroscopy: The Tyrosyl Radical–Diiron Cofactor in Ribonucleotide Reductase from Yeast

Galit Bar, Marina Bennati,* Hiep-Hoa T. Nguyen, Jie Ge, JoAnne Stubbe, and Robert G. Griffin

Contribution from the Center for Magnetic Resonance, Francis Bitter Magnet Laboratory and Department of Chemistry, Massachusetts Institute of Technology, Cambridge, Massachusetts 02139-4307

Received August 21, 2000. Revised Manuscript Received November 28, 2000

Abstract: High-frequency pulsed EPR and ENDOR have been employed to characterize the tyrosyl radical (Y•)–diiron cofactor in the Y2-containing R2 subunit of ribonucleotide reductase (RNR) from yeast. The present work represents the first use of 140-GHz time domain EPR and ENDOR to examine this system and demonstrates the capabilities of the method to elucidate the electronic structure and the chemical environment of protein radicals. Low-temperature spin–echo-detected EPR spectra of yeast Y• reveal an EPR line shape typical of a tyrosyl radical; however, when compared with the EPR spectra of Y• from *E. coli* RNR, a substantial upfield shift of the g_1 -value is observed. The origin of the shift in g_1 was investigated by 140-GHz ^1H and ^2H pulsed ENDOR experiments of the Y2-containing subunit in protonated and D_2O -exchanged buffer. ^2H ENDOR spectra and simulations provide unambiguous evidence for one strongly coupled ^2H arising from a bond between the radical and an exchangeable proton of an adjacent residue or a water molecule. Orientation-selective 140-GHz ENDOR spectra indicate the direction of the hydrogen bond with respect to the molecular symmetry axes and the bond length (1.81 Å). Finally, we have performed saturation recovery experiments and observed enhanced spin lattice relaxation rates of the Y• above 10 K. At temperatures higher than 20 K, the relaxation rates are isotropic across the EPR line, a phenomenon that we attribute to isotropic exchange interaction between Y• and the first excited paramagnetic state of the diiron cluster adjacent to it. From the activation energy of the rates, we determine the exchange interaction between the two irons of the cluster, $J_{\text{exc}} = -85 \text{ cm}^{-1}$. The relaxation mechanism and the presence of the hydrogen bond are discussed in terms of the differences in the structure of the Y•–diiron cofactor in yeast Y2 and other class I R2s.

Introduction

The role of amino acid radicals in the catalytic reaction of numerous enzymes has been well documented in the past few years.¹ The development and application of spectroscopic techniques that access the chemical and electronic structure of such radicals is a crucial step in the study of their function. In this paper, we describe the first use of 140-GHz time domain EPR and ENDOR to characterize the tyrosyl radical (Y•)–diiron cofactor in the subunit R2 of ribonucleotide reductase (RNR) from yeast.

EPR and ENDOR provide data on the hyperfine interaction between unpaired electron spins and surrounding magnetic nuclei and are therefore ideal techniques to obtain structural information on paramagnetic species.² However, EPR and ENDOR experiments at conventional frequencies (9 GHz, 0.35 T) often lead to complex, unresolved spectra. The development of high-frequency EPR technology ($\nu \geq 100 \text{ GHz}$), in combination with time domain methods has greatly increased the accessible information content.^{3,4} First, at high frequencies, it

is possible to perform spectroscopy with sample volumes of a few nanoliters and at concentrations in the range of 10–100 μM . Further, at high magnetic fields, the g -anisotropy of the radicals, as well as the Larmor frequencies of low- γ nuclei, is well resolved and the nuclear frequencies are large compared to the hyperfine couplings. These features permit determination of g -values with a precision of better than $\sim 10^{-4}$, and more accurate analysis of ENDOR spectra, as the spectra are more “first order”. To date, high-frequency ENDOR capabilities have only been demonstrated in a few laboratories at 95 GHz.^{5–7} We have recently described a pulsed EPR/ENDOR spectrometer operating at 140 GHz.⁸ Specifically, we reported ENDOR spectra of the stable Y• in the R2 subunit of RNR from *Escherichia coli*, and we showed that spectra at these frequencies permit an unambiguous assignment of the weakly coupled protons and a determination of their bond orientation with respect to the molecular frame.

In the past few years, the stable Y• in several class I RNRs has been studied extensively with high-frequency EPR.^{8–16} The

* To whom correspondence should be addressed. E-mail: bennati@ccnmr.mit.edu.

(1) Stubbe, J.; Donk, W. A. v. d. *Chem. Rev.* **1998**, 98, 705–762.

(2) Hoff, A. *Advanced EPR, Applications in Biology and Biochemistry*; Elsevier: Amsterdam, 1989.

(3) Lebedev, Y. S. In *Modern Pulsed and Continuous-Wave Electron Spin Resonance*; Kevan, L., Bowman, M. K., Eds.; Wiley Interscience: New York, 1990; pp 365–404.

(4) Prisner, T. F. *Adv. Magn. Opt. Res.* **1997**, 20, 245–283.

(5) Disselhorst, J. A. J. M.; van der Meer, H.; Poluektov, O. G.; Schmidt, J. *J. Magn. Reson.* **1995**, 116, 183–188.

(6) Rohrer, M.; Plato, M.; MacMillan, F.; Grishin, Y.; Lubitz, W.; Möbius, K. *J. Magn. Reson. A* **1995**, 116, 59–66.

(7) Gromov, I.; Krymov, V.; Manikandan, P.; Arieli, D.; Goldfarb, D. *J. Magn. Reson.* **1999**, 139, 8–17.

(8) Bennati, M.; Farrar, C. T.; Bryant, J. A.; Inati, S. J.; Weis, V.; Gerfen, G. J.; Riggs-Gelasco, P.; Stubbe, J.; Griffin, R. G. *J. Magn. Reson.* **1999**, 138, 232–243.

impetus for these investigations is the fact that RNRs play an essential role in cellular DNA biosynthesis and repair by catalyzing the conversion of ribonucleotides to deoxyribonucleotides.^{17–20} Class I RNRs occur in all eukaryotes and in some prokaryotes with the *E. coli* enzyme being the prototype. The enzymes are composed of two subunits designated R1 and R2, R1 contains the active site for nucleotide reduction, and R2 contains a Y•–diiron cluster cofactor that functions as a radical chain initiator required for catalysis. The Y• on R2 is believed to initiate long-range electron-coupled proton transfer and formation of a thiyl radical (S•) in the active site of R1. The S• then initiates the nucleotide reduction process.

Studies in yeast have identified four RNR subunits: two R1s designated Y1 and Y3 and two R2s designated Y2 and Y4.^{21–24} A combination of these subunits is thought to provide the nucleotides required for DNA replication and repair. Genome sequencing projects have revealed that almost all organisms have multiple RNRs. In yeast, Y4 is an unusual subunit as it lacks three of the conserved ligands to the putative diiron center essential for Y• formation. Furthermore, genetic studies revealed that replacement of the tyrosine in Y4, the precursor to the Y•, with a phenylalanine has no effect on the activity of Y4 in vivo. We²⁵ have purified Y2 from *E. coli* and yeast and Y4 from *E. coli*. We demonstrated that Y4 is essential for generation of a Y• in yeast R2, and we and others demonstrated that Y2 and Y4 can exist as a heterodimer in vivo.^{23–25}

The yeast Y• was first observed by Harder and Follmann.²⁶ However, the instability of the radical and RNR activity precluded isolation and detailed characterization of this species. In the present investigation, we report characterization of the reconstituted Y• of yeast R2 generated in the presence of equal amounts of homodimers of Y2 and Y4, ferrous iron, and O₂. Our recent studies suggest that the yeast R2 characterized in this paper is likely to be a heterodimer with one radical per Y2/Y4.²⁷ Our studies support the recent proposal²⁸ on recombinant Y2 and Y4 expressed simultaneously in *E. coli* that the active R2 is a heterodimer composed of a monomer of Y2 and a monomer of Y4.

In this paper, we describe the use of high-frequency ENDOR, which has allowed detection of a hydrogen bond between the Y• and an unknown exchangeable proton. Further, we observe enhanced spin–lattice relaxation rates of this radical which we suggest are associated with an isotropic paramagnetic exchange interaction with the first excited paramagnetic state of the neighboring diiron cluster. The unique features of Y• in yeast Y2 will be discussed in relationship to structural differences with other class I RNR systems.

Materials and Methods

Generation of Yeast R2 Y•. Y4 was isolated from *E. coli* as described previously.²³ Recently, the (His)₆–Y2 was also expressed in *E. coli* and purified using a cobalt affinity column.²⁷ The recombinant Y4 and (His)₆–Y2 isolated from *E. coli* contain no iron and no Y•. The following method was used to reconstitute the diiron–Y• cluster. The (His)₆–Y2 (200 μM) and Y4 (300 μM) in 50 mM Hepes, 15% glycerol (pH 7.4) were deoxygenated by allowing the solutions to equilibrate in an anaerobic box refrigerator (4 °C) for 3 h. A solution of FeSO₄ in the same buffer was deoxygenated as previously described.²⁵ The (His)₆–Y2, Y4, and Fe(II) solutions were then mixed in the anaerobic box to yield a solution containing 20 μM, (His)₆–Y2, 20 μM Y4, and 100 μM FeSO₄. The solution was incubated at 4 °C for 1 h, removed from the anaerobic box, and exposed to air for 15 min. The sample was then concentrated to ~475 μM in protein and used directly in high-field EPR and ENDOR studies. The protein sample was then exchanged into D₂O buffer containing 50 mM Hepes, 15% glycerol-*d*₃ (pD ~ 7.4), concentrated to 550 μM and then used for high-field EPR and ENDOR measurements.

High-Frequency EPR. Samples for 140-GHz EPR and ENDOR spectroscopy consisted a volume of ~250 nL in a Suprasil quartz tube of 0.5 mm outer diameter. EPR spectra at 140 GHz were acquired with a custom-designed high-sensitivity pulsed EPR/ENDOR spectrometer.⁸ The advantage of time domain techniques at our frequency consists first in the elimination of noise and baseline drifts that arise in CW experiments from mechanical coupling of the field modulation coil with the probe. Second, echo-detected EPR (EDEPR) spectra at low temperatures are much less sensitive to saturation effects and analysis of the EPR line shape is more straightforward. Typical $\pi/2$ pulses of 100 ns are achieved by using a high-quality cylindrical cavity modified for ENDOR operation and an incident microwave power of 5 mW. EDEPR spectra were recorded with a standard three-pulse stimulated echo sequence $((\pi/2)_x - \tau - (\pi/2)_x - T - (\pi/2)_x - \tau - \text{echo})$; see the inset in Figure 1) with integration of the echo intensity as the magnetic field is swept. Experimental conditions such as number of accumulated echoes per point, number of field sweeps, and recycle delays were adjusted for different temperatures and are indicated for each case in the figure captions. For magnetic field and *g*-values measurements, we employ an NMR teslameter that continuously detects the ²H NMR signal from a ²H₂O sample.

ENDOR. The Davies ENDOR $((\pi)_x - \text{rf} - (\pi/2)_x - \tau - (\pi)_x - \tau - \text{echo})$ technique was typically used to record ¹H ENDOR spectra, whereas the Mims ENDOR sequence $((\pi/2)_x - \tau - (\pi/2)_x - \text{rf} - (\pi/2)_x - \tau - \text{echo})$ was employed for ²H ENDOR spectra due to its inherently higher sensitivity to small hyperfine couplings. The optimal ENDOR performance was obtained at ~6 K, where the relaxation time (*T*₁ ~ 100 ms) of the Y• permits reasonable signal accumulation rates, while taking advantage of an enhanced Boltzmann population difference. The short spin–spin lattice relaxation time, *T*₂, requires a pulse spacing of $\tau = 160$ ns in the Mims sequence.

Spin–Lattice Relaxation Measurements. *T*₁ measurements were performed using a stimulated-echo-detected saturation recovery technique. The saturation pulse length was set on the order of *T*₁ to suppress spectral diffusion processes that arise from hole burning in the inhomogeneously broadened EPR line.²⁹ A stimulated echo sequence was used instead of a simple two-pulse echo due to the larger excitation bandwidth that leads to larger signal-to-noise ratios. Saturation pulse

(9) Gerfen, G. J.; Bellew, B. F.; Un, S.; Bollinger, J. M.; Stubbe, J.; Griffin, R. G.; Singel, D. J. *J. Am. Chem. Soc.* **1993**, *115*, 6420–6421.

(10) Un, S.; Atta, M.; Fontecave, M.; Rutherford, A. W. *J. Am. Chem. Soc.* **1995**, *117*, 10713–10719.

(11) Allard, P.; Barra, A. L.; Andersson, K. K.; Schmidt, P. P.; Atta, M.; Gräslund, A. *J. Am. Chem. Soc.* **1996**, *118*, 895.

(12) Schmidt, P. P.; Andersson, K. K.; Barra, A. L.; Thelander, L.; Gräslund, A. *J. Biol. Chem.* **1996**, *271*, 23615.

(13) Sauge-Merle, S.; Lauthere, J. P.; Coves, J.; Le Pape, L.; Menage, S.; Fontecave, M. *J. Biol. Inorg. Chem.* **1997**, *2*, 586.

(14) Dam, P. J. v.; Willems, J.; Schmidt, P. P.; Pötsch, S.; Barra, A.; Hagen, W. R.; Hoffman, B. M.; Andersson, K. K.; Gräslund, A. *J. Am. Chem. Soc.* **1998**, *120*, 5080–5085.

(15) Liu, A.; Poetsch, S.; Davydov, A.; Barra, A. L.; Rubin, H.; Gräslund, A. *Biochemistry* **1998**, *37*, 16369.

(16) Liu, A.; Barra, A.; Rubin, H.; Lu, G.; Gräslund, A. *J. Am. Chem. Soc.* **2000**, *122*, 1974.

(17) Stubbe, J. *J. Biol. Chem.* **1990**, *265*, 5329–5332.

(18) Reichard, P. *Science* **1993**, *260*, 1773–1777.

(19) Sjöberg, B.-M. *Struct. Bonding (Berlin)* **1997**, *88*, 139–173.

(20) Stubbe, J. *Proc. Natl. Acad. Sci. U.S.A.* **1998**, *95*, 2723.

(21) Elledge, S. J.; Davis, R. W. *Mol. Cell. Biol.* **1987**, *7*, 2783–2793.

(22) Elledge, S. J.; Davis, R. W. *Genes Dev.* **1990**, *4*, 740–751.

(23) Huang, M.; Elledge, S. J. *Mol. Cell. Biol.* **1997**, *17*, 6105–6113.

(24) Wang, P. J.; Chabes, A.; Casagrande, R.; Tian, X. C.; Thelander, L.; Huffaker, T. *Mol. Cell. Biol.* **1997**, *17*, 6114–6121.

(25) Nguyen, H. T.; Ge, J.; Perlstein, D. L.; Stubbe, J. *Proc. Natl. Acad. Sci. U.S.A.* **1999**, *96*, 12339–12344.

(26) Harder, J.; Follmann, H. *Free Radical Res. Commun.* **1990**, *10*, 281.

(27) Ge, J.; Nguyen, H.-H. T.; Perlstein, D. L.; Stubbe, J., manuscript in preparation.

(28) Chabes, A.; Domkin, V.; Larsson, G.; Liu, A.; Gräslund, A.; Wijmenga, S.; Thelander, L. *Proc. Nat. Acad. Sci., U.S.A.* **1999**, *97*, 2474.

(29) Beck, W. F.; Innes, J. B.; Lynch, J. B.; Brudvig, G. W. *J. Magn. Reson.* **1991**, *91*, 12–29.

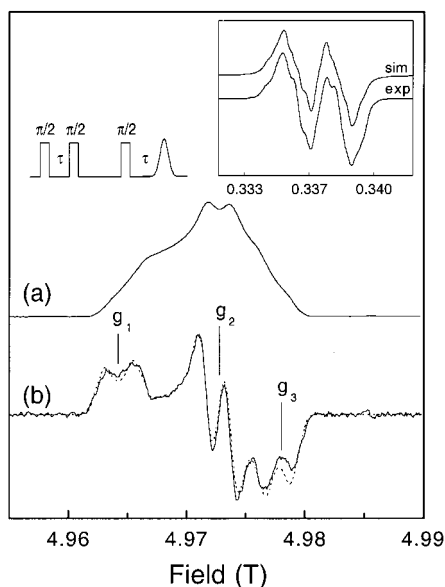


Figure 1. The 140-GHz echo-detected EPR spectrum of $Y\bullet$ in 0.5 mM yeast Y2 (a) at 6 K and its derivative spectrum (b). Experimental parameters: $t_{\pi/2} = 110$ ns, $\tau = 200$ ns, 30 averages/point, and nine spectral scans are averaged. The dotted line is a simulation with g -values (Table 1), and hyperfine parameters as reported in the text. Upper left: stimulated echo pulse sequence used to record the 140-GHz spectrum. Inset: X-band CW EPR spectrum (bottom) and simulation (top).

lengths typically ranged from 10 μ s to 10 ms. The temperature was controlled by an Oxford flow cryostat system (Spectrostat and ITC502 controlling unit) equipped with a resistance temperature device (Lake-shore). To reproducibly establish temperatures of the sample, equilibration for a minimum of 1 h was required at each point. Recovery curves were simulated with least-squares fitting routines available in Kaleida-Graph software.

Spectra Simulations. EPR and ENDOR spectra were simulated using MATLAB routines developed in-house that are based on a first-order Hamiltonian (high-field condition) for the hyperfine and quadrupolar interaction. EPR transition frequencies are accordingly given by

$$\nu_s = \frac{g\beta_e B_0}{h} + \sum_{i=1}^n m_i^i A_{zz}^i \quad (1)$$

where g and A_{zz} are the angular dependent g -factor and hyperfine constant, respectively. The summation runs over i nuclear spins and m_i^i are the nuclear quantum numbers. The quadrupole interaction is neglected for simplicity. The ENDOR transition frequencies for a $I = 1$ quadrupolar nucleus are given by³⁰

$$\begin{aligned} \nu(+) &= |0.5A - \nu \pm 3/2Q_{zz}| \quad \text{and} \\ \nu(-) &= |-0.5A - \nu \pm 3/2Q_{zz}| \quad (2) \end{aligned}$$

where Q_{zz} is the angular dependent quadrupole tensor component in the laboratory frame. For a spin $I = 1$, $Q_{zz} = e^2 q Q / 2$, where e is the electric charge, q the electric field gradient, and Q the scalar quadrupole moment.

To calculate the orientation-selected ENDOR spectra, we first simulate the EPR line shape taking into account g -anisotropy and the full set of hyperfine couplings. In a second step, we select orientations that contribute to the EPR resonance at the given field position inbetween the excitation bandwidth. We approximate the excitation bandwidth of the microwave pulse as a Lorentz function with a frequency width $\delta\nu \approx 1/t_{mw}$ (~ 10 MHz for a 100-ns pulse). The first step, i.e., a good simulation of the EPR line shape, is important for a precise selection of orientations since large hyperfine couplings partially

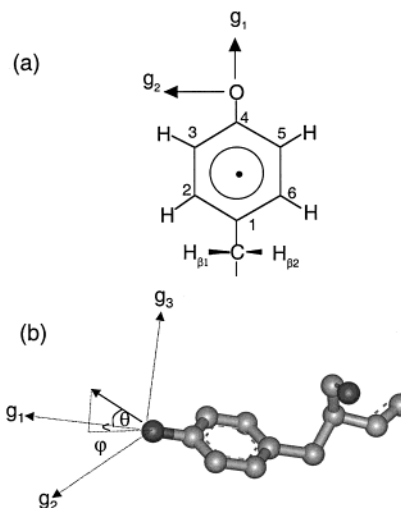


Figure 2. Schematic representation of the tyrosyl radical (a). The direction of the hydrogen bond is indicated by an arrow and related to the molecular symmetry axes represented by the g -tensor principal axis (b).

scramble the orientational selectivity. The ENDOR line shapes were convoluted with a line width approximated by a Lorentz function of width $\delta\nu \approx 1/t_{rf}$, where t_{rf} is the length of the rf pulse.³¹

Results and Discussion

EPR Spectra. The 140-GHz EDEPR spectrum of reconstituted yeast R2 $Y\bullet$ at $T = 6$ K is shown in Figure 1. It displays a typical absorptive powder line shape of a $Y\bullet$ dominated by the anisotropy of the electron Zeeman interaction. A ~ 20 G splitting is visible in the center of the spectrum due to a large hyperfine interaction of one β -methylene proton with the unpaired electron spin. Additional features of the spectrum are visible in the first-derivative line shape plotted in Figure 1b, where the large β -methylene ^1H splitting is also observable on both edges of the powder pattern.

In the 140-GHz EPR spectrum of *E. coli* $Y\bullet$ from Gerfen et al.,⁹ additional hyperfine structure was found superimposed on the low-field edge of the spectrum. The additional structure was assigned to the hyperfine coupling with the three- and five-ring protons (for nomenclature see Figure 2), which in *E. coli* $Y\bullet$ leads to a quintet with intensity ratios 1:2:2:2:1. However, in the case of yeast $Y\bullet$, no further structure is well resolved. We suggest that other sources of broadening might contribute to the 140-GHz EPR spectrum, such as an intermediate size hyperfine couplings or broadening due to a distribution of molecular conformations.

Simulations of the 140-GHz EPR spectrum were performed in order to obtain a set of g -values. These g -values are listed in Table 1 and compared with g -values of other class I RNR tyrosyl radicals. The g -values of the yeast $Y\bullet$ are similar to those of mouse, HSV1, and *Arabidopsis thaliana* RNRs and differ from the tyrosyl radicals of *E. coli*, *Salmonella typhimurium*, and *Mycobacterium tuberculosis*. The agreement with mouse R2 is worth noting, since both enzymes are eukaryotes and display a high percentage of sequence identity in R2.³² The g -values indicate that the electrostatic environments of tyrosyl radicals in mouse and yeast are very similar. For mouse and HSV1 $Y\bullet$, the shift in g_1 with respect to the *E. coli* system has been corre-

(31) Grupp, A.; Mehring, M. Pulsed ENDOR in Solids. In *Modern Pulsed and Continuous-Wave Electron Spin Resonance*; Kevan, L., Bowman, M., Eds.; Wiley Interscience: New York, 1990.

(32) Kauppi, B.; Nielsen, B.; Ramaswamy, S.; Kjoller Larsen, I.; Thelander, M.; Thelander, L.; Eklund, H. *J. Mol. Biol.* **1996**, 262, 706.

(30) Poole, C. P.; Farach, H. A. *The theory of magnetic resonance*; John Wiley & Sons: New York, 1972.

Table 1. Principal g -Values for Various Tyrosyl Radicals in Class I RNR Enzymes

	g_1	g_2	g_3	ref
<i>E. coli</i>	2.00912	2.00457	2.00225	9
<i>S. typhimurium</i>	2.00897	2.00437	2.00217	11
<i>M. tuberculosis</i>	2.0080–92	2.0046	2.0022	16
mouse	2.0076	2.0043	2.0022	12
HSV1	2.0076	2.0043	2.0022	14
<i>A. thaliana</i>	2.0078	2.0043	2.0022	13
yeast	2.00770	2.00435	2.00229	this work

lated with the effect of a hydrogen bond on the oxygen spin density of the tyrosine.¹⁴ Whether this correlation is consistent also for the yeast R2 Y• is discussed in the next section.

The simulation of the high-frequency spectrum includes a set of hyperfine parameters for four coupled protons. Since the 140-GHz EPR line shape is not particularly sensitive to hyperfine couplings smaller than ~ 5 G, the parameter set was optimized to obtain a reasonable representation of the X-band spectrum. The X-band CW spectrum and its simulation are displayed in the inset of Figure 1. The hyperfine parameters used in the simulation in Figure 1 were (in gauss) as follows: $A_x(\beta_1) = 21.0$; $A_y(\beta_1) = 20.5$; $A_z(\beta_1) = 22.0$; $A_x(3,5) = -10.0$; $A_y(3,5) = -4.0$; $A_z(3,5) = -6.0$; $A_x(\beta_2) = 1.8$; $A_y(\beta_2) = 4.1$; $A_z(\beta_2) = 2.9$. The numbers in parentheses correspond to the labeling of the protons in Figure 2. The three largest hyperfine couplings are observed in all RNR tyrosyl radicals, whereas the intermediate size coupling has been reported only for the mouse and HSV1 radicals.^{14,33} Since the spin density distribution on the aromatic ring is not expected to vary substantially between different tyrosyl radicals, it is reasonable to assign the observed intermediate size coupling to the β_2 -methylene proton, the coupling arising from a different dihedral angle between the Y• aromatic plane and the protein backbone.

Deuterium ENDOR Experiments. We performed pulsed ENDOR experiments in an effort to clarify the origin of the g_1 -shift and to identify the magnetic nuclei coupled to the unpaired electron spin. In other RNR systems^{14,16} and in PSII,^{34,35} the g_1 -shift has been correlated with the presence of a hydrogen bond to the oxygen of Y•, and we therefore first recorded ^2H Mims ENDOR spectra of the yeast R2 in D_2O . The observation of a ^2H ENDOR signal with a substantial spectral width ($\Delta\nu_{\text{max}} \sim 1.2$ MHz at $B = 49\,680$ G) provided the first unambiguous evidence that one or more exchangeable ^2H 's are weakly coupled to the unpaired electron spin. For a more precise analysis, the ENDOR spectra were recorded at different field positions across the EPR powder pattern as illustrated in Figure 3.

First, we note that the deuterium ENDOR spectra are highly symmetric around the Larmor frequency, as expected at our operating field of 5 T, where the nuclear frequency of deuterium ($\omega_L/2\pi$ (^2H) = 32.2 MHz) is much larger than the observed hyperfine splitting (weak coupling regime). The spectra reveal a substantial orientation dependence that arises from the anisotropic hyperfine interaction. At all orientations, we observe a doublet of doublets characteristic of a hyperfine and quadrupole splitting of a single deuterium spin. The line shape, however, is more complex due to the contributions of several molecular orientations. Only for microwave excitation at the edges $B = g_1$ and $B = g_3$ of the EPR line shape are the ENDOR powder patterns reduced to "single crystal" like spectra.

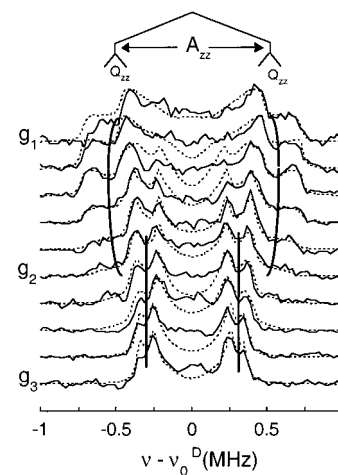


Figure 3. ^2H Mims-ENDOR spectra of yeast Y• in D_2O buffer recorded across the EPR line (solid lines) and simulations (dashed lines). The field positions $B = g_1$, g_2 , and g_3 correspond to the values marked in Figure 1. Experimental parameters: $T = 6$ K, $t_{\text{rf}} = 100$ ns, $\tau = 160$ ns, $t_{\text{rf}} = 70$ μs , rf power = 1 kW, 100 shots/point, and two scan average per spectrum. Simulation parameters are reported in Table 2. For a better illustration, the angular dependence of the dominant hyperfine coupling is traced by a solid line.

To determine the hyperfine tensor of the deuteron and its relative orientation with respect to the g -tensor principal axes, a simulation of the field-dependent data set is required. For one coupled deuteron, we assume coaxial hyperfine and quadrupole tensors and an axially symmetric hyperfine tensor. The first assumption is based on the observation that maximum and minimum hyperfine and quadrupole splitting occurs at the same excitation positions in the EPR line and we expect that the unique axis of the hyperfine tensor points along the bond direction.³⁴ The simulation then involves seven independent parameters, i.e., two hyperfine tensor components (A_{iso} and A_{\perp} with $2A_{\perp} = -A_{\parallel}$), two quadrupole tensor components (traceless tensor), and three Euler angles (φ , θ , ψ) that define a rotation of the hyperfine and quadrupole tensors into the g -tensor principal axis system. A starting parameter set was estimated by evaluating the observed maximum and minimum hyperfine and quadrupolar splitting from the experimental data, i.e., $A_{\text{max}} = 1.2$ MHz, $A_{\text{min}} = 0.6$ MHz, $Q_{\text{max}} = 0.08$ MHz, and $Q_{\text{min}} = 0.02$ MHz. ENDOR simulations were performed by systematically varying the Euler angles first in 20° steps and then in smaller steps ($\pm 5^\circ$) around the optimal fit, starting with the unique axis of the hyperfine tensor parallel to g_1 and varying its direction toward g_2 and g_3 . We found that the simulation of the field-dependent data set is very sensitive ($\pm 3^\circ$) to the choice of the Euler angles. The best parameter set is listed in Table 2, and the simulation is plotted with dotted lines on the experimental data of Figure 3. We note that the simulation also considers the effect of the Mims ENDOR preparation function that modulates the ENDOR spectrum $I(\omega)$ according to $I(\omega) \sim 1 - \cos[(\omega - \omega_L)\tau]$, where τ is the interpulse spacing and $\omega_L/2\pi$ is the free Larmor frequency. For a spacing $\tau = 160$ ns, the function burns a hole in the center of the ENDOR spectrum but does not produce additional blind spots in the observed hyperfine coupling range (± 1.5 MHz). Since spectral diffusion during the rf pulse affects the shape of the hole, the hole was approximated by a Lorentzian line shape³⁶ with an optimized width of 0.7 MHz.

(33) Hoganson, C. W.; Babcock, G. T. *Biochemistry* **1992**, *31*, 11874–11880.

(34) Force, D. A.; Randall, D. W.; Britt, R. D.; Tang, X. S.; Diner, B. *J. Am. Chem. Soc.* **1995**, *117*, 12643.

(35) Farrar, C. T.; Force, D. A.; Gerfen, G. J.; Britt, R. D.; Griffin, R. G. *J. Phys. Chem. B* **1997**, *101*, 6634–6641.

(36) Höfer, P. Ph.D. Thesis, University of Stuttgart, Stuttgart, Germany, 1988.

Table 2. Principal Hyperfine and Quadrupole Values with Their Orientations Used in the Simulations of the 140-GHz ^2H ENDOR Spectra and Comparison with Literature Data of Mouse and HSV1 Y• from Van Dam et al.¹⁴

	yeast	mouse	HSV1
A_1 (MHz)	1.20	1.06	1.12
A_2 (MHz)	−0.6	−0.53	−0.56
A_3 (MHz)	−0.6	−0.53	−0.56
Q_1 (MHz)	0.08	0.07	0.07
Q_2 (MHz)	−0.06	−0.05	−0.05
Q_3 (MHz)	−0.02	−0.02	−0.02
θ	20	20	20
φ	25	0	40
ψ	0	0	0
r (Å)	1.81	1.89	1.86

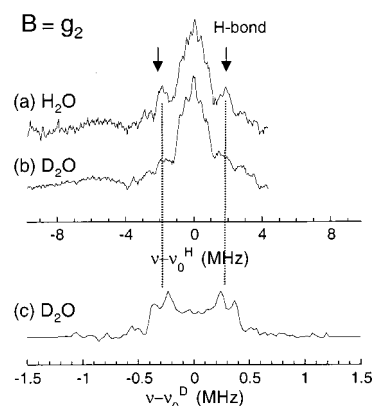
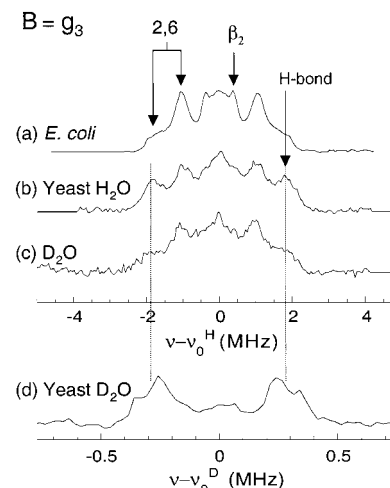
The excellent agreement between experiment and simulation illustrates the capability of high-field orientation selective ENDOR spectra in constraining the fitting parameters and allowing accurate determination of the hyperfine tensor and its spatial orientation. To determine the bond direction, the g -tensor is oriented in the molecule with the largest component g_1 pointing along the C–O bond of the Y• and the smallest component g_3 perpendicular to the Y• ring plane (Figure 2) as described by Gerfen et al.⁹ On the other hand, as mentioned above, we expect the unique axis of the dipolar hyperfine tensor to point along the O–D bond. Thus, according to our Euler angles, the hydrogen bond is rotated by $\theta = 20^\circ$ out of the ring plane and by $\varphi = 25^\circ$ away from the C–O bond in the ring plane. The bond orientation is illustrated by the arrow in Figure 2b.

The bond length can be estimated from a point dipole model, where the dipole interaction between the nucleus of the deuteron and the electron spin density on the oxygen is considered. In such a point dipole model, the perpendicular hyperfine tensor component is inversely proportional to the cube of the dipole distance r :

$$A_{\perp} = \frac{\mu_0}{4\pi} g_e \beta_e g_n \beta_n \rho_o \frac{1}{r^3} \quad (3)$$

here ρ_o is the unpaired electron spin density on the oxygen and g and β are the nuclear and electronic g -factors and magnetons, respectively. From eq 3, it is evident that the accuracy of the calculated distance depends not only on the error of the experimentally determined hyperfine coupling but also on the knowledge of the spin density at the oxygen, which is unknown for the yeast Y•. However, theoretical calculations^{35,37} show similar oxygen spin densities, around 0.3, for all tyrosyl radicals and suggest that the hydrogen bond affects the spin density on the oxygen by less than 15%. For our estimates and comparison with literature data, we assume a spin density of 0.3 and we obtain a bond length of 1.81 Å.

Finally, we compare our results on the yeast Y• with previous data on the mouse and HSV1 RNRs Y• from 35-GHz ENDOR studies of Dam et al.¹⁴ The data for all three enzymes are assembled in Table 2. The magnitude of the deuterium hyperfine couplings agree within 5%. The hyperfine coupling in the yeast Y• is slightly larger than in the mouse and HSV1. Accordingly, the calculation of the bond length results in a shorter distance for yeast Y•, 1.81 versus 1.86 Å in Y• of mouse and 1.89 Å in Y• of HSV1 (Table 2). In all three cases, the oxygen spin densities are unknown and the same value of $\rho_o = 0.3$ has been

**Figure 4.** ENDOR spectra of yeast Y• recorded in the center of the EPR spectrum at $B = 49\,730$ G ($g = 2$). (a) Davies ^1H ENDOR spectrum of Y• in protonated buffer and (b) in D_2O buffer. Experimental parameters: $T = 15$ K, $t_{\pi} = 200$ ns, $t_{\text{rf}} = 10$ μs , rf power = 400 W, 100 shots/point, and single scan spectra. (c) ^2H Mims ENDOR spectrum of Y• in D_2O recorded at the same magnetic field position. Experimental parameters are reported in Figure 3.**Figure 5.** ^1H ENDOR spectra (a–c) of *E. coli* and yeast Y• recorded at $B = 49\,785$ G ($B = g_3$). (a) *E. coli* Y• in H_2O buffer, (b) yeast Y• in H_2O buffer, and (c) yeast Y• in D_2O buffer. Experimental parameters as in Figure 4. (d) ^2H Mims ENDOR spectrum of yeast Y• in D_2O recorded at the same magnetic field position. Experimental parameters as in Figure 3.

assumed. Thus, the reported bond lengths might be affected by an error of about 10–15%.

The results suggest that the hydrogen bond is rotated out of the ring plane by an angle $\theta = 20^\circ$ in all three systems. However, there is some difference between the parameters that represent the C–O–H angle: our value of $\varphi = 25^\circ$ is intermediate between that of mouse and of HSV1 Y•. Whether the discrepancy is due to an experimental uncertainty or reflects a real difference in chemical environment is presently unknown since the uncertainty for the mouse and HSV1 data is likely much higher than in our experiment due to the lower orientation selectivity at 1 (35 GHz) versus 5 T (140 GHz).

Proton ENDOR Spectra. We have recorded ^1H -Davies ENDOR spectra of the yeast R2 Y• in protonated buffers to better understand the proton hyperfine coupling and the electronic structure. Due to technical limitations in tuning our ^1H resonant circuit over a 20-MHz range, we restrict the proton ENDOR analysis to the small coupling region ($A < |10|$ MHz). In Figures 4 and 5, we display ^1H -Davies ENDOR spectra of yeast Y• at field positions $B = g_2$ and $B = g_3$, respectively.

(37) Himo, F.; Gräslund, A.; Eriksson, L. A. *Biophys. J.* **1997**, 72, 1556–1567.

The proton spectra are compared with the deuterium spectra, where the frequency axis has been multiplied by a factor of $\gamma_{\text{H}}/\gamma_{\text{D}} = 6.5$. In both Figures 4 and 5 we observe that the hydrogen bond contributes to peaks at ± 1.9 MHz at field positions $B = g_2$ and $B = g_3$, consistent with an axially symmetric hyperfine tensor. The intensity of these peaks decreases in the ^1H ENDOR when the sample is in deuterated buffer and reappears at the corresponding scaled frequency in the ^2H spectra.

At field position $B = g_3$, Figure 5, we also compare the yeast $\text{Y}\bullet$ ^1H ENDOR spectrum with the *E. coli* $\text{Y}\bullet$ ENDOR spectrum from Bennati et al.⁸ In the *E. coli* analysis, we have demonstrated that orientation selection at this field position leads to spectra that are highly resolved and amenable to computational analysis. In the *E. coli* $\text{Y}\bullet$ spectrum, Figure 5a, the shoulders at ± 2 MHz display a shape similar to those of yeast Y in deuterated buffer, Figure 5c, whereas the yeast ^1H spectrum in H_2O , Figure 5b, shows more pronounced peaks at around ± 1.9 MHz arising from the H-bond. The observation is consistent with the absence of a hydrogen bond in the *E. coli* $\text{Y}\bullet$. Further, in the *E. coli* spectrum the relevant features have been previously attributed⁸ to the 2,6 and the β_2 -methylene protons, as illustrated in Figure 5a. However, in the yeast $\text{Y}\bullet$ spectrum b, we expect that only the 2,6 and not the β_2 -methylene protons contribute to the small coupling region ($A < |10|$ MHz), since simulations of the X-band EPR spectrum indicate that the hyperfine coupling of the β_2 -methylene proton is of the order of 10–15 MHz. Indeed, in this ^1H ENDOR experiment with yeast R2, we fail to observe the doublet at ± 0.5 MHz, observed in the *E. coli* spectrum and assigned to the β_2 -methylene proton. In contrast, the second more intense doublet at ± 1.0 MHz and the shoulders at ± 2.1 MHz are observed in both systems. This result clearly supports our assignments of the β_2 -methylene proton and of the 2,6 protons, in particular that the intense doublet and the shoulders both arise from the 2,6 protons.

Relaxation Behavior of $\text{Y}\bullet$. One of the most interesting features in the X-band CW EPR of yeast $\text{Y}\bullet$ was discussed previously by Harder and Follmann.²⁶ In particular, they reported that the signal associated with the $\text{Y}\bullet$ was observed only at temperatures below 60 K. We have confirmed this observation and additionally noted the onset of substantial line broadening at temperatures above 15 K. This behavior is unique to the yeast $\text{Y}\bullet$, since the CW spectra of *E. coli* and mouse $\text{Y}\bullet$ have been detected at room temperature and 200 K, respectively.³⁸ To better understand this observation, we have investigated the spin–lattice relaxation time, T_1 , of the $\text{Y}\bullet$ at 140 GHz using stimulated echo-detected saturation recovery. The spin–lattice relaxation of *E. coli* and other class I RNR tyrosyl radicals has been studied in detail by CW³⁸ and pulse methods at X-band frequencies.^{39,40} In the latter experiments, nonexponential saturation recovery curves were observed below 60 K and attributed to the anisotropic magnetic dipolar interaction between $\text{Y}\bullet$ and the lowest paramagnetic excited state ($S = 1$) of the diiron cluster. These studies have provided the basis for analysis of the data described subsequently.

Saturation recovery curves for the yeast and *E. coli* $\text{Y}\bullet$ were recorded for $T < 60$ K at different field positions of the 140-GHz EPR line shape. Typical recovery curves acquired in the center of the EPR line are displayed in Figure 6. All curves are monoexponential above 15 K, as is visible in the figure where

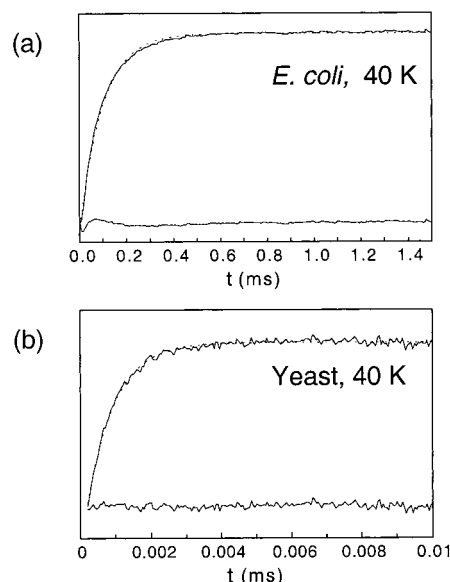


Figure 6. Typical saturation recovery curves of *E. coli* (a) and yeast (b) $\text{Y}\bullet$ recorded at $T = 40$ K and $B = g_2$. Note the difference in the time scale of the x-axis. The experimental data are represented by solid lines, least-squares fits with a monoexponential function are dashed lines, and the residuals (difference between experimental curve and fits) are displayed at the bottom of each plot.

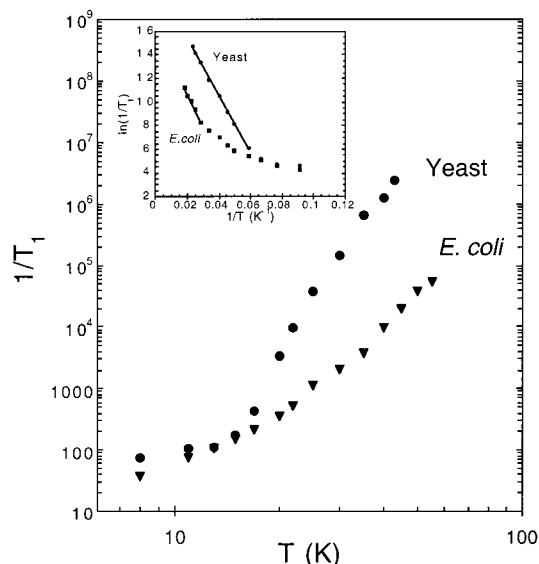


Figure 7. $1/T_1$ spin–lattice relaxation rates obtained from monoexponential least-squares fits of saturation recovery curves at $B = g_1$. Dots represent data for yeast and triangles for *E. coli* $\text{Y}\bullet$. Inset: $\ln(1/T_1)$ versus $1/T$ plots for yeast and *E. coli* $\text{Y}\bullet$. The straight lines are linear least-squares fit to the data. The resulting slopes are discussed in the text.

we show monoexponential fits and their residuals. No dependence of the recovery was observed on the length of the saturating pulse, which was set at each temperature to be $\sim 5T_1$. Least-squares fits were performed in order to obtain the electronic spin–lattice relaxation time, T_1 , and the resulting rates $1/T_1$ at $B = g_1$ are displayed in Figure 7.

The temperature dependence of $1/T_1$ presented in Figure 7 provides evidence for enhanced relaxation in yeast $\text{Y}\bullet$ above 15 K. Furthermore, for $T \geq 30$ K, the relaxation rates of yeast $\text{Y}\bullet$ are ~ 2 orders of magnitude larger than for *E. coli* $\text{Y}\bullet$. To obtain additional insight into the relaxation mechanism of yeast $\text{Y}\bullet$, we plot $\ln(1/T_1)$ as a function of $1/T$ for both yeast and *E. coli* $\text{Y}\bullet$, (Figure 7, inset). Note the linear behavior characteristic

(38) Sahlin, M.; Petersson, L.; Gräslund, A.; Ehrenberg, A.; Sjöberg, B.-M.; Thelander, L. *Biochemistry* **1987**, 26, 5541.

(39) Hirsh, D. J.; Beck, W. F.; Lynch, J. B.; Que, L.; Brudvig, G. W. *J. Am. Chem. Soc.* **1992**, 114, 7475.

(40) Galli, C.; Atta, M.; Andersson, K. K.; Gräslund, A.; Brudvig, G. J. *Am. Chem. Soc.* **1995**, 117, 740.

Table 3. Spin Lattice Relaxation Rates $1/T_1$ (s^{-1}) of $Y\bullet$ in Yeast Y2 Determined at Different Field Positions of the 140-GHz EPR Line^a

B (G)	$1/T_1$ at 10 K ($\times 10^1 s^{-1}$)	$1/T_1$ at 20 K ($\times 10^3 s^{-1}$)	$1/T_1$ at 30 K ($\times 10^5 s^{-1}$)	$1/T_1$ at 40 K ($\times 10^6 s^{-1}$)
49 650	8.15	3.11	1.33	1.08
49 700	9.02	3.18	1.42	1.25
49 730	10.6	3.26	1.44	1.28
49 800	7.85	3.21	1.44	1.22

^a The experimental error amounts to $\sim 3\%$.

of a thermally activated process, with an onset temperature of 15 K in yeast and ~ 35 K in *E. coli*. As mentioned above, for *E. coli* and other class I RNRs, the thermally activated process has been unambiguously related to the population of the first ($S = 1$) paramagnetic state of the diiron cluster. The exchange Hamiltonian of the two coupled spins S_1 and S_2 , i.e., $H = -2J_{\text{exc}}S_1S_2$, yields the energy separation between two spin states of $E(S) = -J_{\text{exc}}S(S + 1)$, where S is the total spin state and J_{exc} the exchange coupling. Using the activation energies derived from the slopes of the straight lines (Figure 7), and assuming that the activation energy equals $2J_{\text{exc}}$, the spacing between the $S = 0$ and $S = 1$ states of the diiron cluster (subsequently denoted Fe_2 for simplicity), we can calculate $J_{\text{exc}}^{\text{yeast}}(\text{Fe}_2) = -85 \text{ cm}^{-1}$ and $J_{\text{exc}}^{\text{E.coli}}(\text{Fe}_2) = -95 \text{ cm}^{-1}$. The latter is in excellent agreement with the value reported by Hirsch et al.³⁹ at 9 GHz ($J_{\text{exc}}^{\text{E.coli}}(\text{Fe}_2) = -94 \text{ cm}^{-1}$) and from static magnetic measurements ($J_{\text{exc}}^{\text{E.coli}}(\text{Fe}_2) = -108 \text{ cm}^{-1}$).⁴¹ Since the activation energies in yeast and *E. coli* are very similar, we conclude that the relaxation enhancement in yeast $Y\bullet$ is also caused by paramagnetic relaxation by the diiron cluster.

With this information, we can further probe whether the mechanism of paramagnetic relaxation is governed by dipolar or exchange interaction. At 140 GHz, the EPR line shape is dominated by g -anisotropy and molecular orientations are easy to select using a typical excitation bandwidth of 3–4 G (100 ns $\pi/2$ pulse). Accordingly, orientational selectivity permits discrimination between a relaxation mechanism governed by an anisotropic versus a scalar interaction. For an isotropic mechanism, $1/T_1$ rates are independent of the orientations and thus equal across the EPR line, leading to monoexponential recovery curves. In contrast, an anisotropic mechanism is reflected in different rates across the EPR line and is expected to lead to some degree of nonmonoexponentiality in the recovery curves at field positions far from the outer canonical orientations.

We report in Table 3 typical $k_1 = 1/T_1$ values of yeast $Y\bullet$ determined at four representative field positions across the EPR line. The rates observed at 10 K are determined by the “intrinsic relaxation” of $Y\bullet$ in the absence of a fast relaxing spin (the paramagnetic diiron cluster). These values are clearly anisotropic and ~ 2 orders of magnitude smaller than in the thermally activated region. Also, the recovery curves in this temperature range ($T < 15$ K) were not strict monoexponential. In contrast, at $T = 20$ K the anisotropy of k_1 , which we define as $k_1(g_3)/k_1(g_1)$, lies within the experimental error of $\sim 3\%$. Specifically, at $T = 30$ and 40 K, $k_1(g_3)/k_1(g_1)$ is about 1.08 and 1.18, respectively, and thus increases only slightly with temperature. Rates determined at five additional field positions, for $T > 15$ K, displayed very similar values. As mentioned previously, all recovery curves above 15 K were monoexponential. For comparison, we have repeated the same experiments with the *E. coli* $Y\bullet$ and also in this case we observe minimal differences between the rates across the EPR line above 20 K.

The results strongly indicate that the relaxation mechanism in the thermally activated region is dominated by an isotropic

interaction. We note that these results, particularly the *E. coli* case, are considerably different from what has been reported for *E. coli*,³⁹ mouse, and HSV1⁴⁰ $Y\bullet$ at 9 GHz. For *E. coli*, mouse, and HSV1, anomalous nonexponential recoveries were observed and interpreted in terms of anisotropic relaxation, where different molecular orientations lead to a superposition of angular dependent T_1 recovery curves. The k_1 rate was determined to vary by a factor of 3–4 with the molecular orientation. The origin of the discrepancy between the observation of anisotropic versus isotropic relaxation at low and high frequency is likely due to the different dynamic range of spin–lattice relaxation at 140 versus 9 GHz. However, details are not yet understood and a deeper theoretical investigation and additional data at different frequencies are required to characterize the spectral density functions. Nevertheless, we believe that the 140-GHz data on yeast and *E. coli* are self-consistent to allow a further analysis. Indeed, our observation of an anisotropy in T_1 at low temperatures demonstrates that its absence at higher temperatures is not an experimental artifact. In contrast, it additionally supports our interpretation that anisotropic relaxation is negligible at higher temperatures due to a dominant isotropic mechanism.

The concomitant observation of an isotropic and a thermally activated relaxation rate strongly suggests that the dominant mechanism for enhanced relaxation in yeast $Y\bullet$ is the isotropic exchange interaction with the diiron cluster. An evaluation of this interaction can be performed using the theory first described by Abragam⁴³ together with a few additional assumptions. This approach was applied to RNR $Y\bullet$ by Hirsch et al.³⁹ The exchange relaxation between a slowly and a rapidly relaxing spin is given by

$$k_{\text{lexc}} = \frac{2J_{\text{exc}}^2(Y\bullet - \text{Fe}_2)\mu_{\text{eff}}^2}{3g_f^2\beta^2} \frac{T_{2f}}{1 + (\omega_s - \omega_f)^2 T_{2f}^2} \quad (4)$$

where μ_{eff} is the effective magnetic moment of the diiron cluster and the subscripts s and f correspond to the slow and fast relaxing spins, respectively. Unfortunately, $J_{\text{exc}}(Y\bullet - \text{Fe}_2)$ cannot be determined from the rate without knowledge of the Lorentzian function $T_{2f}/(1 + (\omega_s - \omega_f)^2 T_{2f}^2)$. However, we can estimate the ratio $J_{\text{exc}}^{\text{E.coli}}(Y\bullet - \text{Fe}_2)/J_{\text{exc}}^{\text{yeast}}(Y\bullet - \text{Fe}_2)$ by a comparison of rates and by assuming the Lorentzian function in eq 4 to be similar for the two enzymes. Solving eq 4 for $J_{\text{exc}}^{\text{E.coli}}(Y\bullet - \text{Fe}_2)/J_{\text{exc}}^{\text{yeast}}(Y\bullet - \text{Fe}_2)$ gives

$$\frac{J_{\text{exc}}^{\text{E.coli}}(Y\bullet - \text{Fe}_2)}{J_{\text{exc}}^{\text{yeast}}(Y\bullet - \text{Fe}_2)} \approx \sqrt{\frac{k_{\text{lexc}}^{\text{E.coli}}\mu_{\text{eff}}^2(\text{yeast})}{k_{\text{lexc}}^{\text{yeast}}\mu_{\text{eff}}^2(\text{E.coli})}} \quad (5)$$

The ratio of the effective magnetic moments can be approximated by³⁹

$$\frac{\mu_{\text{eff}}^2(\text{yeast})}{\mu_{\text{eff}}^2(\text{E.coli})} \approx \frac{\exp(2J_{\text{exc}}^{\text{yeast}}(\text{Fe}_2)/kT)}{\exp(2J_{\text{exc}}^{\text{E.coli}}(\text{Fe}_2)/kT)} \quad (6)$$

This ratio can be calculated at each temperature from the determined exchange couplings of the diiron cluster $J_{\text{exc}}(\text{Fe}_2)$ in yeast and *E. coli*. Inserting the experimental $k_1(\text{E.coli})/k_1(\text{yeast})$

(41) Petersson, L.; Gräslund, A.; Ehrenberg, A.; Sjöberg, B.-M.; Reichard, P. *J. Biol. Chem.* **1980**, *255*, 6706.

(42) Hirsh, D. J.; Beck, W. F.; Innes, J. B.; Brudvig, G. W. *Biochemistry* **1992**, *31*, 532.

(43) Abragam, A. *Principles of Nuclear Magnetism*; Clarendon Press: Oxford, 1961.

ratios (Figure 7) and the μ_{eff}^2 ratios for two temperatures in eq 5 gives at $T = 35$ K, $J_{\text{exc}}^{\text{E.coli}}(\text{Y}\bullet - \text{Fe}_2)/J_{\text{exc}}^{\text{yeast}}(\text{Y}\bullet - \text{Fe}_2) = 0.12$ and at $T = 40$ K, 0.14. Since $J_{\text{exc}}(\text{Y}\bullet - \text{Fe}_2)$ is temperature independent, the average value results to 0.13.

Our estimates indicate that $J_{\text{exc}}(\text{Y}\bullet - \text{Fe}_2)$ in yeast is substantially larger than in *E. coli* R2. If we consider $|J_{\text{exc}}^{\text{E.coli}}(\text{Y}\bullet - \text{Fe}_2)|$ of 0.0047 cm^{-1} determined for *E. coli* by Hirsch et al.,³⁹ the exchange coupling in yeast Y2 should be on the order of 0.04 cm^{-1} . The differences in exchange coupling require differences in the structural features of the $\text{Y}\bullet - \text{Fe}_2$ cofactors.

Some insight into what factors could effect such changes are obtained by examining well-characterized exchange coupled metal ion/organic radical systems reported in the literature. One well-characterized system is the transient $(\text{Fe}=\text{O})^{2+}$ heme-tryptophan cation radical cofactor found in cytochrome *c* peroxidase.^{44–46} A second system is the $\text{Fe}(\text{II})$ -quinone radical acceptor complex in a bacterial reaction center that is involved in photosynthesis.^{47,48} In the first case, the $S = 1$ spin of the oxyferryl $(\text{Fe}=\text{O})^{2+}$ heme moiety is exchange coupled to the $S = 1/2$ tryptophan cation radical (Trp191) situated $\sim 5 \text{ \AA}$ apart.⁴⁴ EPR data⁴⁵ gave evidence for an unusually broad EPR signal that could be simulated with a distribution of J couplings in the range -0.049 to $+0.098 \text{ cm}^{-1}$. The most distinguishing feature of this system is the presence of a hydrogen bond network between the heme and Trp191, which is essential for the observation of the exchange coupling, as pointed out by Goodin and McRee⁴⁶ in their studies of mutant peroxidases.

In the reaction center of *Rhodospseudomonas sphaeroides*, the $\text{Fe}(\text{II})$ center is located $\sim 8 \text{ \AA}$ from the closest quinone radical (Q_B).⁴⁷ The EPR spectrum⁴⁸ of the exchanged coupled system is extremely broad (from $g = 2$ to $g < 0.8$) and could be simulated with an anisotropic tensor ($J_x = -0.09$, $J_y = -0.41$, and $J_z = -0.41 \text{ cm}^{-1}$), corresponding to an isotropic exchange coupling of $J = -0.30 \text{ cm}^{-1}$. Also in this case, a hydrogen bond network between the quinones and two histidines (His M219 and His L190) coordinated to the iron center was reported.⁴⁷ The similarities between these systems and the yeast Y2 cofactor in terms of distance, magnitude of J coupling, and presence of a hydrogen bond network is provocative. Since in yeast the magnitude of the J coupling depends on the spatial overlap of the electron wave function of $\text{Y}\bullet$ and Fe_2 , the comparison might suggest that the detected hydrogen bond in yeast $\text{Y}\bullet$ is directed to a water molecule coordinated to the Fe1 of the diiron cluster. This hypothesis has been also formulated by Dam et al.¹⁴ for mouse and HSV1 R2 cofactors but based only on the observation of the H-bond. The estimated enhancement in J coupling in yeast Y2 $\text{Y}\bullet$ relative to the *E. coli* $\text{Y}\bullet$ suggests that the Fe1 of the diiron center in the yeast case has an appropriately positioned water which is absent or in a different position in the latter case.

If the proposed model to explain the relaxation properties of the yeast $\text{Y}\bullet$ is correct, then the question arises as to whether an exchanged coupled EPR signal in the $\text{Y}\bullet - \text{Fe}_2^*$ ($S_1 = 1/2$, $S_2 = 1$, the star denotes the first excited state of Fe_2) system is observable. The signal is expected to be very broad and weaker than in the above-mentioned systems, since the paramagnetic

states of the Fe_2 cluster are excited only at higher temperatures. Further, fast relaxation from the paramagnetic into the diamagnetic state would lead to additional lifetime broadening. Due to the limited sweep range of the 5-T magnet in our 140-GHz spectrometer (approximately $1.8 \leq g \leq 2.2$), we are not able to address this question. However, it should be possible using a standard X-band spectrometer and is being investigated. The disappearance of the yeast $\text{Y}\bullet$ CW EPR signal above 60 K, observed to date only in yeast Y2 and not in other class I RNR R2s, could be related to the magnitude of the $J_{\text{exc}}(\text{Y}\bullet - \text{Fe}_2)$ coupling and to the concomitant appearance of an exchanged coupled broadened EPR signal at another field region.

Conclusions

We have reported a high-frequency (140-GHz) EPR/ENDOR investigation on the $\text{Y}\bullet$ from yeast R2. The 140-GHz EPR spectra display g -values that are very similar to those of other eukaryotic systems and differ from those of prokaryotic R2s. The 140-GHz pulsed ENDOR spectroscopy was used to further describe the electrostatic and chemical environment of $\text{Y}\bullet$. Yeast R2 $\text{Y}\bullet$ was examined in D_2O , and we found evidence for one weakly coupled deuteron to $\text{Y}\bullet$. The excellent orientation selectivity of 140-GHz ENDOR spectra allowed us to determine the hyperfine coupling between the radical and the deuteron and the hyperfine tensor orientation with respect to the molecular axis. From the hyperfine coupling, we have estimated a bond length of 1.81 \AA and calculated bond orientations: $\theta = 20 \pm 3^\circ$ and $\varphi = 25 \pm 3^\circ$.

Spin-lattice relaxation measurements were performed in an effort to understand the differences in the behavior of the yeast $\text{Y}\bullet$ in comparison with other class I RNR tyrosyl radicals, that is, the disappearance of the CW EPR signal above 60 K. The rates $k_1 = 1/T_1$ obtained from orientationally selected recovery curves provide evidence for thermally activated relaxation above 15 K and no significant relaxation anisotropy. The results have been interpreted in terms of a relaxation mechanism governed by isotropic paramagnetic exchange coupling between the $\text{Y}\bullet$ and the diiron cluster.

A comparison with other well-characterized exchange-coupled metal ion/organic radicals suggests that the enhanced relaxation might be correlated with the presence of the detected hydrogen bond and that the bond is formed to a water molecule coordinated to the Fe1 of the diiron cluster. Although such a relaxation enhancement has been consistently observed in the literature in H-bonded RNR tyrosyl radicals, i.e., to date in mouse, HSV1, and yeast, the magnitude of the exchange coupling might vary substantially between these systems. The magnitude of the $J_{\text{exc}}(\text{Y}\bullet - \text{Fe}_2)$ coupling is expected to be sensitive to structural parameters such as the $\text{Y}\bullet - \text{Fe}_2$ distance and the hydrogen bond network. Differences in J coupling could be correlated with the different features observed in mouse, HSV1, and yeast, i.e., the shorter H-bond distance and different H-bond orientation in yeast versus mouse and HSV1. The disappearance of the CW EPR signal above 60 K, observed uniquely in yeast $\text{Y}\bullet$, suggests that the isotropic exchange interaction between $\text{Y}\bullet$ and Fe_2 is stronger in yeast than in other class I RNR R2s.

Acknowledgment. The project was supported by grants from the National Institutes of Health (GM-38395, GM-29595, RR-00995). Thanks are accorded to Jeff Bryant for his assistance in the construction and maintenance of the 140-GHz EPR/ENDOR spectrometer. M.B. would like to thank G. Gerfen for helpful discussions.

JA003108N

(44) Finzel, B. C.; Poulos, T. L.; Kraut, J. *J. Biol. Chem.* **1984**, *259*, 13027.

(45) Houseman, A. L. P.; Doan, P. E.; Goodin, D. B.; Hoffman, B. M. *Biochemistry* **1993**, *32*, 4430.

(46) Goodin, D. B.; McRee, D. E. *Biochemistry* **1993**, *32*, 3313.

(47) Allen, J. P.; Feher, G.; Yeates, T. O.; Komiya, H.; Rees, D. C. *Proc. Natl. Acad. Sci. U.S.A.* **1988**, *85*, 8487.

(48) Butler, W. F.; Calvo, R.; Fredkin, D. R.; Isaacson, R. A.; Okamura, M. Y.; Feher, G. *Biophys. J.* **1984**, *45*, 947.